AIMS Mathematics, 10(12): 30307–30330.
DOI:10.3934/math.20251331
Received: 02 November 2025
Revised: 11 December 2025
Accepted: 17 December 2025
Published: 24 December 2025

https://www.aimspress.com/journal/Math

Research article

New solutions to the (3+1)-dimensional HB equation using bilinear neural networks method and symbolic ansatz method using neural network architecture

Jianglong Shen[1,*], **Min Liu**[1,*], **Jingbin Liang**[1] **and Runfa Zhang**[2,*]

[1] Department of Mathematics and Physics, Yibin University, college street, Yibin 644000, Sichuan, China

[2] School of Automation and Software Engineering, Shanxi University, Wucheng street, Taiyuan 030013, China

* **Correspondence:** Email: jlshen@yibinu.edu.cn, 1996104001@yibinu.edu.cn, zrf@sxu.edu.cn.

Abstract: This study introduces a novel hybrid computational framework that synergistically integrates neural networks with symbolic computation to address nonlinear partial differential equations (PDEs). By combining the robust nonlinear approximation capabilities of neural networks with the analytical precision of symbolic computation, our proposed symbolic ansatz method using neural network architecture (SANNA) achieves superior accuracy and efficiency compared to conventional numerical techniques. With in this framework, we design three distinct neural network architectures—each incorporating varied trial functions—and further integrate the bilinear neural network method (BNNM). To validate the effectiveness of our methodology, we apply it to the (3+1)-dimensional HB equation, a prototypical nonlinear model with significance in soliton theory and wave dynamics. The approach yields multiple novel analytical solutions, including periodic traveling waves and strongly localized nonlinear modes, all exhibiting clear mathematical interpretability and physical relevance. These results highlight the method's potential for applications in fluid dynamics, ocean engineering, and geophysical flow modeling.

Keywords: neural network; nonlinear dispersion; trial function method; symbolic computation; soliton solutions
Mathematics Subject Classification: 35A25, 35Q51

1. Introduction

PDEs have widespread applications in various fields such as mathematics, physics, engineering, biomedicine, and earth sciences. In the process of constructing and solving actual models, handling

PDEs derived from real-world problems is a common and critical task. By solving these equations and analyzing the properties and patterns of their solutions, researchers can gain a deep understanding of the intrinsic characteristics and external phenomena of the objects under study. Therefore, finding appropriate solution methods has become a core component of model construction and problem-solving. With the continuous development of PDE theory, solution methods have become increasingly diverse. Scholars have conducted in-depth research on various phenomena in daily life, leading to the development of many novel and effective solution methods. These methods not only advance theoretical research but also provide powerful tools for practical applications.

Currently, scholars have studied and developed various classical and novel approaches for solving PDEs, including the combination of physics-informed neural networks and interpolation polynomials [1], the deep hybrid residual method [2], and the use of PINNs [3]. The Hirota bilinear equation is primarily used to describe complex systems such as wave systems and is widely applied in soliton theory to derive soliton solutions for nonlinear PDEs. It can transform various nonlinear equations, such as the Korteweg-de Vries (KdV) equation [4], the (3+1)-dimensional Hirota-Satsuma-Ito (HSI) equation [5], the (2+1)-dimensional Yu-Toda-Sasa-Fukuyama (YTSF) equation [6], and the Schrödinger-Hirota equation [7], into the Hirota bilinear form, making it easier to solve them. These solutions are typically expressed as polynomials of simple exponential functions. Additionally, it enables the characterization of phenomena and mathematical models in fields such as electromagnetism, heat conduction, acoustics, and fluid mechanics.

This paper will study the Hirota bilinear equation in (3+1) dimensions, whose equation form is

$$u_{yt} - u_{xxxy} - 3u_{xx}u_y - 3u_xu_{xy} - 3u_{xx} + 3u_{zz} = 0. \tag{1.1}$$

Recent research has yielded significant progress in the investigation of bilinear Hirota-type equations. Scholars have researched and obtained various effective analytical and numerical solution methods for Hirota bilinear equations, providing theoretical and methodological guidance for subsequent research on Hirota bilinear equations. Wang et al. [8] obtained N-soliton solutions for the generalized variable coefficient fifth-order KdV equation utilizing the bilinear Hirota technique. Zhou [9] and others extended the linear superposition principle to both standard and generalized bilinear formulations and demonstrated various instances of mixed resonant solitons and complex-valued solutions in the context of bilinear differential systems. Gao et al. [10] transformed the (3+1)-dimensional nonlinear evolution equation into the Hirota bilinear form with dependent variable transformation and obtained non resonant-type one-, two-, and three-wave solutions. Ren et al. [11] constructed two solitary waves based on the Hirota bilinear form. Lan et al. [12] constructed single and double soliton solutions utilizing Hirota's bilinear scheme, and [13] derived dark first-, second-, and third-wave soliton solutions employing Hirota's technique with dual auxiliary functions in bilinear formulation. Gao et al. [14] derived both sufficient and necessary conditions governing the linear superposition principle's validity for exponential traveling waves in Hirota bilinear systems. Utilizing these criteria, the authors constructed an innovative bilinear equation where the superposition principle was effectively employed, leading to the discovery of dual categories of resonant multi-wave solutions. Ma et al. [15] investigated when the Hirota bilinear equation has a linear subspace of solutions. Li et al. [16] formulated a novel dynamical system model, referred to as the (3+1)-dimensional Hirota-type bilinear equation (HBLE), and employed the generalized bilinear Hirota formalism to acquire the (3+1)-dimensional solution of this new HBLE. Ye et al. [17] developed an efficient algorithm

to transform the logarithmic form of KdV-type bilinear equations into Hirota bilinear form; Hajar et al. [18] used Hirota's bilinear method and the long-wave technique for examining the dynamical properties of the proposed equations; Zheng et al. [19] examined the superposition properties of hyperbolic and trigonometric solutions in Hirota bilinear systems, seeking to derive a specialized class of N-soliton solutions expressed through mixed hyperbolic-trigonometric combinations; and Yin et al. [20] studied the variable-coefficient (3+1) generalized shallow-water wave equation (GSWE) using an improved Hirota bilinear method. Literature [21–23] have additionally employed the bilinear approach for a solution of the corresponding equations. Mandal et al. [24] considered the generalized extended form of the multidimensional Hirota bilinear equations, revealing nonlinear wave behaviors in shallow water systems, marine environments, and optical media.

The evolution of computational capabilities has driven innovative analytical and numerical techniques for differential equations. Guo et al. [25] utilized PINNs to resolve time-dependent PDEs, Tang et al. [1] combined PINNs with interpolation polynomials to solve nonlinear PDEs, while Li et al. [26] employed the Hirota bilinear method combined with PINN deep learning technology to investigate machine learning approaches for the HSI-like equation obtained from block wave solutions. Lei et al. [3] used physical information convolutional neural networks to solve PDEs on a sphere, while Bihlo et al. [27] trained PINNs to satisfy differential equations along with specified initial and boundary data.

Significant advances have been achieved by applying neural networks to PDE solutions. Zhang et al. [28] used deep neural networks to solve elliptic PDEs in complex regions, Admon et al. [29] developed an advanced computational framework for fractal-fractional differential equations utilizing deep neural architectures with multiple hidden layers, and Muhammad et al. [30] investigated broader implementations of neural networks for nonlinear PDE solutions. Yi et al. [31] compared and developed two types of recurrent neural networks (RNNs) and utilized the online solution of the steady-state and non-steady-state coefficients of the famous Lyapunov matrix equation. But unlike the aforementioned neural network methods, many scholars have taken a different approach to solving exact solutions, using symbolic computation to directly solve the exact solutions of equations. Lan [32] ,based on the Hirota method, established the bilinear form of the equation using Bell polynomials and combined symbolic computation to construct the N-arc solutions of the equation. Shen et al. [33] studied the nonlinear equations of shallow water waves, proposed three bilinear automatic reverse transformations based on the Hirota method, and by applying Hirota's approach, multiple arc solutions were generated through symbolic calculations. Kumar and others [34] used symbolic computation tools to visualize the dynamic behavior of anomalous wave solutions with different center parameters. Wang [35], Hosseini [36], Jalil [37], and others also used the symbolic computation tool Maple to derive closed-form solutions of nonlinear PDEs. Drawing on the mentioned machine learning and symbolic calculation methods, multiple scholars have merged the two methodologies. Zhang et al. [38] proposed a novel hybrid method of merging bilinear neural networks with symbolic computation to compute exact solutions of nonlinear PDEs, representing the inaugural implementation of neural networks for exact solution derivation. Subsequently, Zhang et al. studies effectively applied the combined bilinear neural network and symbolic computation technique to obtain precise analytical solutions in [39]. Isah et al. [40] used different activation functions provided by various neural network models to derive generalized collective solutions and exact solutions that applied the hybrid bilinear neural network and symbolic computation methodology. Huang et al. [41] introduced a novel symbolic

computation method based on the bilinear neural network method, improving the original bilinear method and proposing a new method for automatically building analytical solutions for nonlinear differential equations. Similar to the aforementioned bilinear methods rooted in neural networks, this area has been extensively studied in the literature; therefore, a detailed elaboration is omitted here. It is worth highlighting that the work of M. Sharifi et al. [42–44] on hybrid nanofluidic-thermal energy systems serves as an excellent exemplar of applying neural networks to address contemporary engineering challenges, thereby providing a valuable roadmap for our future research in this domain.

Currently, the aforementioned methods still face several bottlenecks that require breakthroughs in practical applications. Machine learning-based training models and PINN frameworks often have high requirements for hardware computational resources, which significantly limits their engineering practicality. Regarding traditional numerical methods, their application requires researchers to have a solid foundation in mathematical theory, a barrier that poses significant challenges for beginners and interdisciplinary researchers when adopting these methods. The existence of these issues not only reflects the current challenges in the development of PDE solving technology but also points to the key areas that future research should focus on breaking through.

2. Symbolic ansatz method using neural network architecture (SANNA)

We present a novel neural network framework combining symbolic computation to address nonlinear PDEs, as depicted in Figure 1.

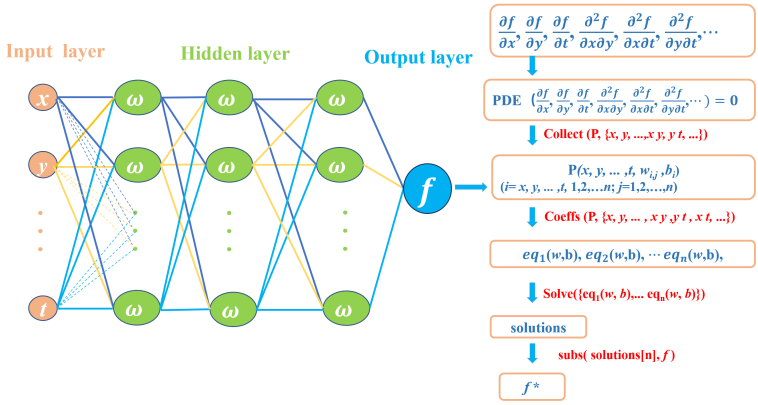

Figure 1. Neural network symbolic computation flow chart.

The framework proposed for solving nonlinear PDEs consists of the following key steps:

Step 1: Model Construction. Construct a feedforward neural network model, whose functional expression serves as the trial solution f(x, y, z, t) for the original PDE.

Step 2: Expression Substitution. Substitute the neural network trial function into the governing PDE, thereby transforming the PDE into an algebraic form containing network parameters (weights and biases).

Step 3: Symbolic Expansion and Coefficient Extraction. Expand the resulting expression symbolically using the expand operation. Then, extract the coefficients corresponding to each derivative term via the coeffs command. This yields a system of algebraic equations relating the network parameters.

Step 4: Parameter Constraint Solving. Solve the obtained system of coefficient equations—often under-determined or coupled—to determine the admissible values of the weights W and biases B. This step effectively enforces the PDE constraints on the network parameters.

Step 5: Analytical Solution Derivation. Substitute the constrained parameter set back into the original neural network expression from Step 1, resulting in an exact, closed-form analytical solution of the PDE.

Step 6: Solution Verification. Finally, substitute the derived analytical solution back into the original PDE to numerically or symbolically verify that the equation is satisfied identically, thereby confirming the correctness of the obtained solution.

Based on the new framework we have constructed, we have designed the following three core solution frameworks: Model(4-2-1) (Figure 2a), Model(4-3-1) (Figure 2b), and Model(4-4-3-1) (Figure 2c).

$$\begin{cases} f = W_{1,f}\,\omega_1(v_1) + W_{2,f}\,\omega_2(v_2) + b_4, \\ v_1 = W_{x,1}x + W_{y,1}y + W_{z,1}z + W_{t,1}t + b_2, \\ v_2 = W_{x,2}x + W_{y,2}y + W_{z,2}z + W_{t,2}t + b_3. \end{cases} \tag{2.1}$$

$$\begin{cases} f = W_{1,f}\,\omega_1(v_1) + W_{2,f}\,\omega_2(v_2) + W_{3,f}\,\omega_3(v_3) + b_4, \\ v_1 = W_{x,1}x + W_{y,1}y + W_{z,1}z + W_{t,1}t + b_2, \\ v_2 = W_{x,2}x + W_{y,2}y + W_{z,1}z + W_{t,2}t + b_3, \\ v_3 = W_{x,3}x + W_{y,3}y + W_{z,1}z + W_{t,3}t. \end{cases} \tag{2.2}$$

$$\begin{cases} f = \sum_{n=5}^{7} W_{n,f}\,\omega_n(v_n) + b_8, \\ v_i = W_{1,i}\omega_1(v_1) + W_{2,i}\omega_2(v_2) + W_{3,i}\omega_3(v_3) + W_{4,i}\omega_4(v_4), \quad i = 5, 6, 7, \\ v_1 = W_{x,1}x + W_{y,1}y + W_{z,1}z + W_{t,1}t + b_1, \\ v_2 = W_{x,2}x + W_{y,2}y + W_{z,2}z + W_{t,2}t + b_2, \\ v_3 = W_{x,3}x + W_{y,3}y + W_{z,3}z + W_{t,3}t + b_3, \\ v_4 = W_{x,4}x + W_{y,4}y + W_{z,4}z + W_{t,4}t + b_5. \end{cases} \tag{2.3}$$

Equation (2.1) is an expression constructed based on a single-hidden-layer neural network model (Figure 2a), and Eq (2.2) is also an expression constructed based on a single-hidden-layer neural network model (Figure 2b). Equation (2.3) is an expression constructed based on a two-hidden-layer neural network model (Figure 2c). Based on the three core neural network frameworks, Model(4-2-1) (Figure 2a), Model(4-3-1) (Figure 2b), and Model(4-4-3-1) (Figure 2c), we adopt different activation function combination strategies to construct three different neural network configurations, thereby obtaining three different detection functions. Multiple new solutions are obtained through the SANNA and bilinear neural network method (BNNM).

Before using BNNM to solve equations, we perform the following linear transformation on the initial equations:

$$u = 2(\ln f)_{xx}. \tag{2.4}$$

After transformation, we obtain the following Hirota bilinear representation of the initial equation:

$$D_xD_yD_tf\cdot f-D_x^3D_yf\cdot f-3D_x^2f\cdot f+3D_z^2f\cdot f+3D_xD_yf\cdot f=0. \tag{2.5}$$

That is

$$\begin{aligned} &f\cdot f_{xyt}-f_xf_{yt}-f_yf_{xt}+f_tf_{xy}-\left(f\cdot f_{xxxy}-3f_xf_{xxy}+3f_{xx}f_{xy}-f_{xxx}f_{xy}\right)\\ &-3\left(f\cdot f_{xx}-f_x^2\right)-3\left(f\cdot f_{zz}-f_z^2\right)+3\left(f\cdot f_{xy}-f_xf_y\right)=0. \end{aligned} \tag{2.6}$$

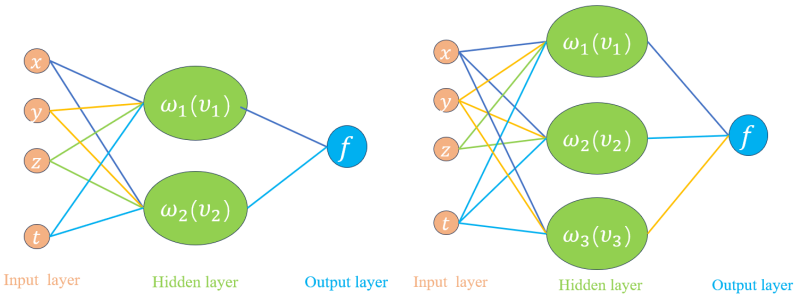

(a) Model(4-2-1) (b) Model(4-3-1)

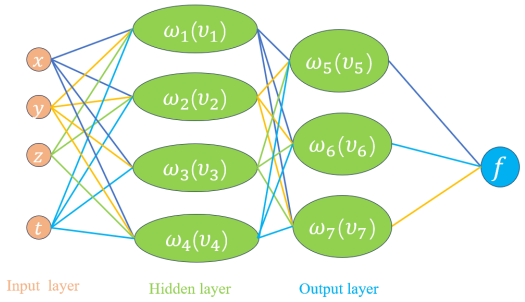

(c) Model(4-4-3-1)

Figure 2. The neural network model.

3. Single-hidden-layer model

3.1. Model(4-2-1)

3.1.1. Model(4-2-1)-Case 1

To derive the exact solution for the (3+1)-dimensional HB equation, we first select a single-hidden-layer model (Figure 2a), in which the input layer consists of x, y, z, t and the hidden layer consists of two neurons

$$\omega_1(v_1), \omega_2(v_2).$$

In the context of this model construction, we set the activation functions in the neural network to be

$$\omega_1(v_1)=\operatorname{sech}(v_1)^2,\ \omega_2(v_2)=\cos(v_2). \tag{3.1}$$

Based on the analytical expression provided by the neural network model Model(4-2-1), we can obtain the probe function under this model:

$$\begin{aligned} f = b_4 + W_{1,u}[\mathrm{sech}(tW_{t,1} + xW_{x,1} + yW_{y,1} + zW_{z,1} + b_2)]^2 \\ + W_{2,u}\cos(tW_{t,2} + xW_{x,2} + yW_{y,2} + zW_{z,1} + b_3). \end{aligned} \tag{3.2}$$

Substituting Eq (3.2) into the transformed partial differential Eq (1.1), we obtain the following solution:

$$\begin{cases} b_3 = b_3, \\ t = t, \quad x = x, \quad y = y, \quad z = z, \\ W_{1,u} = W_{1,u}, \quad W_{2,u} = 0, \\ W_{t,1} = -\dfrac{W_{z,1}^2}{W_{y,1}}, \quad W_{t,2} = -\dfrac{W_{z,1}^2}{W_{y,2}}, \\ W_{x,1} = 0, \quad W_{x,2} = 0, \\ W_{y,1} = W_{y,1}, \quad W_{y,2} = W_{y,2}, \\ W_{z,1} = W_{z,1}. \end{cases} \tag{3.3}$$

Substituting Eq (3.3) into Eq (3.2), we obtain an exact solution to the initial equation, which is expressed as follows:

$$f = b_4 + W_{1,u}\,\mathrm{sech}\left(\frac{yW_{y,1}^2 + (zW_{z,1} + b_2)\,W_{y,1} - tW_{z,1}^2}{W_{y,1}}\right)^2 + W_{2,u}\cos\left(-\frac{tW_{z,1}^2}{W_{y,2}} + yW_{y,2} + zW_{z,1} + b_3\right). \tag{3.4}$$

The model is structured as a single-hidden-layer network (4-2-1), with activation functions $sech^2$ and cos, capturing the behavior of a linearly dominated periodic traveling wave. Physically, this solution corresponds to small-amplitude periodic waves in shallow water, where the nonlinear term ($sech^2$) introduces weak modulation, while the linear term (cos) ensures wave stability. Weight parameters $W_{y,1}$ and $W_{z,1}$: These govern the wave propagation direction and the wave-number. An increase in $W_{z,1}$ raises the wave-number along the z-direction, leading to a shorter wavelength. The ratio $W_{y,1}/W_{z,1}$ determines the inclination angle of the wave vector. The parameter constraint $W_{t,1} = -W_{z,1}^2/W_{y,1}$ reflects that the wave velocity v is governed by $W_{z,1}^2/W_{y,1}$, indicating that the square of the wave speed is directly dictated by this weight ratio. Bias terms b_2 and b_3: These represent phase shifts. Specifically, b_2 influences the initial position of the soliton component, while b_3 adjusts the phase of the periodic component. The term b_4 acts as a global bias, which can be interpreted as a background field (the mean water level in shallow water wave models). Amplitude modulation parameters $W_{1,u}$ and $W_{2,u}$: These govern the intensity of the soliton and periodic components, respectively. Figure 3 illustrates a three-dimensional graph, contour plot, thermal map, and evolution plot. The waveform exhibits regular periodic oscillations, and the elliptical contour lines indicate wavefront symmetry. The thermal map visualizes the spatial distribution of amplitude through color gradients, and the evolution plot confirms the stability of wave propagation over time. Collectively, these features characterize the behavior of periodic traveling waves under weakly nonlinear conditions.

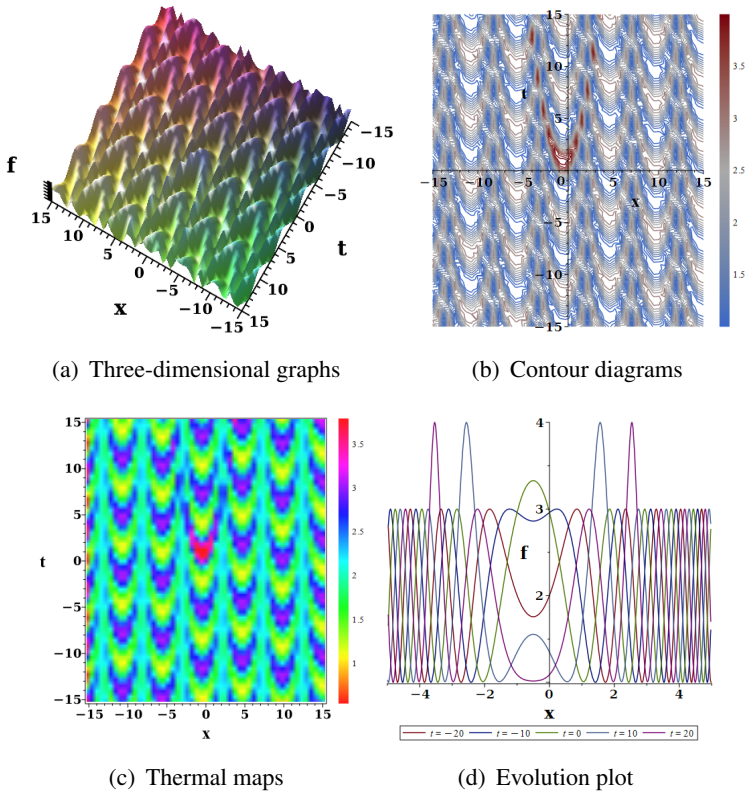

(a) Three-dimensional graphs (b) Contour diagrams

(c) Thermal maps (d) Evolution plot

Figure 3. Three-dimensional graphs, contour diagrams, thermal maps, and evolution plot of Eq (3.4).

3.1.2. Model(4-2-1)-Case 2

Similar to Model(4-2-1)-Case 1, we choose the same activation function.

$$\omega_1(v_1), \omega_2(v_2).$$

Furthermore, the test function is consistent with the test function obtained in Case 1 and is

$$\begin{aligned} f = {} & b_4 + W_{1,u}\left[\operatorname{sech}\left(tW_{t,1} + xW_{x,1} + yW_{y,1} + zW_{z,1} + b_2\right)\right]^2 \\ & + W_{2,u}\cos\left(tW_{t,2} + xW_{x,2} + yW_{y,2} + zW_{z,1} + b_3\right). \end{aligned} \tag{3.5}$$

Substituting Eq (3.5) into Eq (1.1) yields a solution similar to Case 1. Here, we select a different solution as follows:

$$\begin{cases} b_3 = b_3, \\ t = t, \quad x = x, \quad y = y, \quad z = z, \\ W_{1,u} = W_{1,u}, \quad W_{2,u} = 0, \\ W_{t,2} = W_{t,2}, \\ W_{x,1} = 0, \quad W_{x,2} = W_{x,2}, \\ W_{y,1} = W_{y,1}, \quad W_{y,2} = W_{y,2}, \\ W_{z,1} = W_{z,1}, \\ W_{t,1} = -\dfrac{W_{z,1}^2}{W_{y,1}}. \end{cases} \tag{3.6}$$

Substituting Eq (3.6) into Eq (3.5), we obtain the solution to the initial equation, which is expressed as follows:

$$f = b_4 + W_{1,u}\,\mathrm{sech}\left(\frac{yW_{y,1}^2 + (zW_{z,1} + b_2)W_{y,1} - tW_{z,1}^2}{W_{y,1}}\right)^2. \tag{3.7}$$

After obtaining Eq (3.7), it was verified that the solution represented by Eq (3.7) satisfies the equation. This solution corresponds to a reduced case derived from the single-hidden-layer model (4-2-1), which accentuates the dominant contribution of the nonlinear term. Physically, it resembles a soliton solution in shallow-water wave theory, where nonlinearity leads to energy localization, while the linear term, through parameter constraints, ensures steady-state propagation. Figure 4 displays the waveform of a single soliton. In the three-dimensional plot, the wave packet exhibits pronounced localization. The contour lines are closely spaced, reflecting a compact structure, and the corresponding heatmap confirms that energy is concentrated near the wave crest. The evolution diagram demonstrates that the wave-packet preserves its shape during propagation, characteristic of a steady traveling wave.

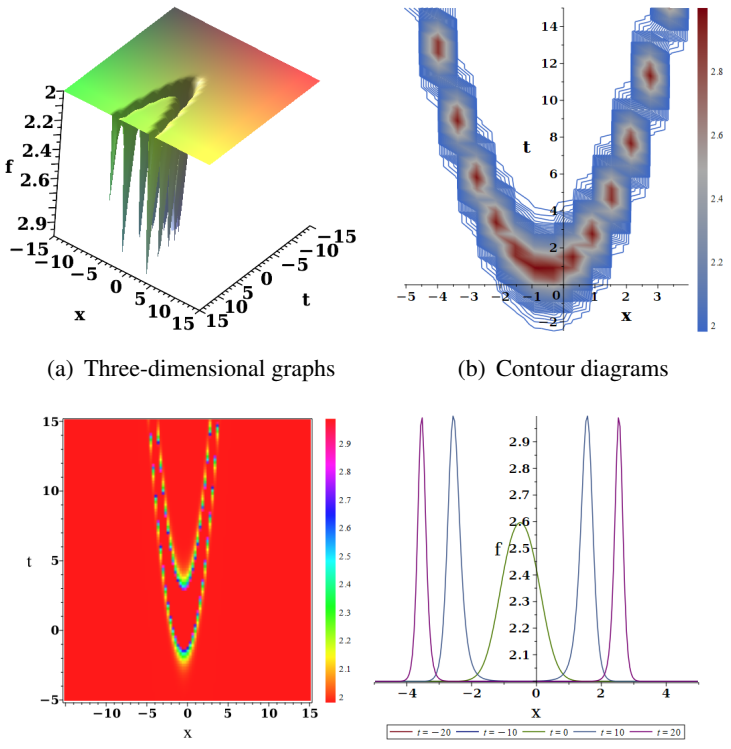

(a) Three-dimensional graphs (b) Contour diagrams

(c) Thermal maps (d) Evolution plot

Figure 4. Three-dimensional graphs, contour diagrams, thermal maps, and evolution plot of Eq (3.7).

From the analysis of the solutions obtained above, it can be seen that, unlike the solutions in Case 1, the behavior of the solutions exhibits localized steady-state characteristics dominated by linear terms, which are typical steady-state traveling wave solutions. However, unlike typical traditional periodic traveling waves, the nonlinear terms have a more pronounced perturbation on the solutions obtained in Case 2, but this perturbation helps the solutions maintain steady-state equilibrium.

3.1.3. Model(4-2-1)-Case 3

Model(4-2-1)-Case 1 and Model(4-2-1)-Case 2 used direct neural network symbolic computation. In Model(4-2-1)-Case 3, we try to use a bilinear neural network method to solve the equations.

$$\begin{aligned} f = {} & b_4 + W_{1,u}\left[\operatorname{sech}\left(tW_{t,1} + xW_{x,1} + yW_{y,1} + zW_{z,1} + b_2\right)\right]^2 \\ & + W_{2,u}\cos\left(tW_{t,2} + xW_{x,2} + yW_{y,2} + zW_{z,1} + b_3\right). \end{aligned} \tag{3.8}$$

Substituting Eq (3.8) into Eq (2.6), we select a different solution as follows:

$$\begin{cases} b_3 = b_3, \\ t = t, \quad x = x, \quad y = y, \quad z = z, \quad b_4 = 0, \\ W_{1,u} = 0, \quad W_{2,u} = W_{2,u}, \\ W_{t,1} = W_{t,1}, \quad W_{t,2} = W_{t,2}, \\ W_{x,1} = W_{x,1}, \quad W_{x,2} = W_{x,2}, \\ W_{z,1} = W_{z,1}, \\ W_{y,1} = \dfrac{3(W_{x,2}^2 + W_{z,1}^2)}{W_{x,2}(4W_{x,2}^2 + 3)}. \end{cases} \tag{3.9}$$

Substituting Eq (3.9) into Eq (3.8), we obtain the solution, as follows:

$$u = W_{2,u}\cos\left(tW_{t,2} + xW_{x,2} + \frac{3y(W_{x,2}^2 + W_{z,1}^2)}{W_{x,2}(4W_{x,2}^2 + 3)} + zW_{z,1} + b_3\right). \tag{3.10}$$

Substituting Eq (3.10) into Eq (2.4), we can get the expression of f as follows:

$$f = -2W_{x,2}^2\sec\left(tW_{t,2} + xW_{x,2} + 3y\frac{W_{x,2}^2 + W_{z,1}^2}{W_{x,2}(4W_{x,2}^2 + 3)} + zW_{z,1} + b_3\right)^2. \tag{3.11}$$

This solution of Eq (3.11) is obtained via the bilinear neural network method (BNNM) employing a cosine activation function, capturing the modulated dynamics of periodic waves in a nonlinear medium. Within the context of shallow-water wave theory, such a model can describe adjustments in wave velocity induced by variations in bottom topography. The parameters $W_{x,2}$ and $W_{z,1}$ govern the wavenumber along the x- and z-directions, respectively. Their ratio determines the anisotropy of wave propagation. Figure 5 illustrates the spatially and temporally non-uniform distribution of the wave field. The three-dimensional plot displays alternating wave crests and troughs. Contour lines reveal the curvature of the wavefront, while the corresponding heatmap highlights regions of high (red) and low (blue) wave amplitude, indicating waveform deformation during propagation.

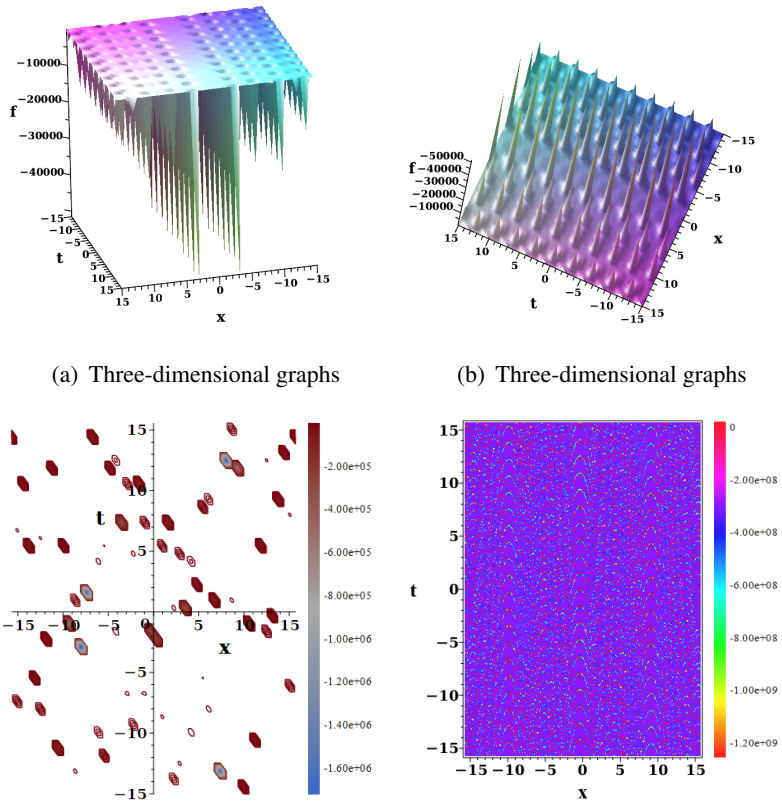

(a) Three-dimensional graphs (b) Three-dimensional graphs

(c) Contour diagrams (d) Thermal maps

Figure 5. Three-dimensional graphs, contour diagrams and thermal maps of Eq (3.11).

3.2. Model(4-3-1)

3.2.1. Model(4-3-1)-Case 1

Following the neural network architecture from Section 3.1, we employ a single-hidden-layer network (Figure 2b) integrated with symbolic computation for equation solving. While maintaining the single-layer structure, we expand the hidden layer's neuron count to three in this implementation. These three neurons are

$$\omega_1(v_1), \omega_2(v_2), \omega_3(v_3).$$

We set the activation function in the neural network as

$$\omega_1(v_1) = \operatorname{sech}^2(v_1), \quad \omega_2(v_2) = \sin(v_2), \quad \omega_3(v_3) = \wp(v_3;\, g_2 = 1,\, g_3 = 1). \tag{3.12}$$

Using our developed neural network architecture Model(4-3-1), we derive the subsequent test function:

$$\begin{aligned} f = {} & b_4 + W_{1,u}\left[\operatorname{sech}\left(tW_{t,1} + xW_{x,1} + yW_{y,1} + zW_{z,1} + b_2\right)\right]^2 \\ & + W_{2,u}\sin\left(tW_{t,2} + xW_{x,2} + yW_{y,2} + zW_{z,1} + b_3\right) \\ & + W_{3,u}\,\wp\left(tW_{t,3} + xW_{x,3} + yW_{y,3} + zW_{z,1};\, g_2 = 1,\, g_3 = 1\right). \end{aligned} \tag{3.13}$$

Substituting Eq (3.13) into Eq (1.1), we obtain the following solution:

$$\begin{cases} b_3 = b_3, \\ t = t, \quad x = x, \quad y = y, \quad z = z, \\ W_{1,u} = W_{1,u}, \quad W_{2,u} = W_{2,u}, \quad W_{3,u} = 0, \\ W_{t,1} = -\dfrac{W_{z,1}^2}{W_{y,1}}, \quad W_{t,2} = -\dfrac{W_{z,1}^2}{W_{y,2}}, \quad W_{t,3} = W_{t,3}, \\ W_{x,1} = 0, \quad W_{x,2} = 0, \quad W_{x,3} = W_{x,3}, \\ W_{y,1} = W_{y,1}, \quad W_{y,2} = W_{y,2}, \quad W_{y,3} = W_{y,3}, \\ W_{z,1} = W_{z,1}. \end{cases} \tag{3.14}$$

By inserting Eq (3.14) into Eq (3.13), we obtain an exact solution of Eq (1.1):

$$\begin{aligned} f = b_4 + W_{1,u}\left[\operatorname{sech}\left(\frac{yW_{y,1}^2 + (zW_{z,1} + b_2)W_{y,1} - tW_{z,1}^2}{W_{y,1}}\right)\right]^2 \\ + W_{2,u}\sin\left(-\frac{tW_{z,1}^2}{W_{y,2}} + yW_{y,2} + zW_{z,1} + b_3\right). \end{aligned} \tag{3.15}$$

Derived from the single-hidden-layer architecture (4-3-1) with $sech^2$ and sine activation functions, this solution embodies the coupling between linear and nonlinear dynamical terms. In a physical context, it can model wave-particle interactions in plasmas, where the sinusoidal component represents periodic external perturbations. The weights $W_{y,1}$ and $W_{z,1}$ govern the wave velocity and wavenumber. The inclusion of a sine function in the activation introduces an explicit phase term. The bias terms b_2 and b_3 modulate the relative phase between the soliton and the periodic components, while b_4 sets a constant background offset. Figure 6 illustrates the superposition of a periodic traveling wave and a localized modulation. The three-dimensional plot exhibits regular oscillations with slight amplitude modulation. The contour lines indicate a uniformly propagating wavefront, while the corresponding heatmap reveals a more complex energy distribution compared to Figure 3. The evolution diagram confirms the stable propagation of the composite waveform.

The wavenumber is governed by the parameters $W_{x,2}$ and $W_{z,1}$. The use of the cosecant (csc) activation function introduces a mathematical singularity into the solution, which can be interpreted physically as corresponding to a resonance condition in the wave field. The coefficient $W_{t,2}$ controls the temporal frequency of oscillation, while the bias b_3 provides a constant phase shift. This solution is obtained via the BNNM. The presence of the cosecant function signifies a strong nonlinear response within the model, which in physical systems—such as shallow-water wave theory—may describe incipient wave breaking or resonant wave interactions. Figure 7 illustrates the rapid spatial oscillations of the wave field and its behavior in the vicinity of the resonant singularity. In the three-dimensional representation, the wave amplitude exhibits divergence at discrete spatial points. The contour lines adopt a radial pattern, and the accompanying heatmap reveals localized regions of very high amplitude, collectively characteristic of a nonlinear resonance.

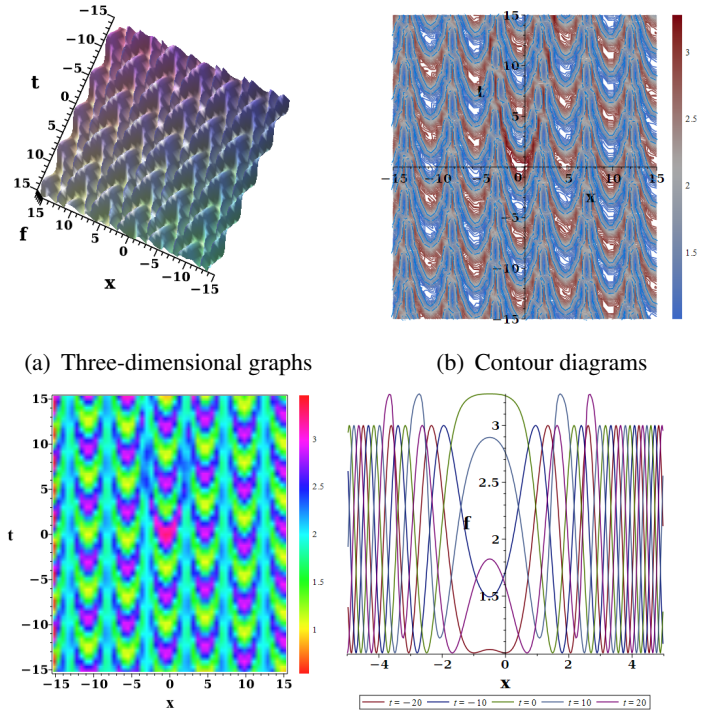

(a) Three-dimensional graphs (b) Contour diagrams

(c) Thermal maps (d) Evolution plot

Figure 6. Three-dimensional graphs, contour diagrams, thermal maps, and evolution plot of Eq (3.15).

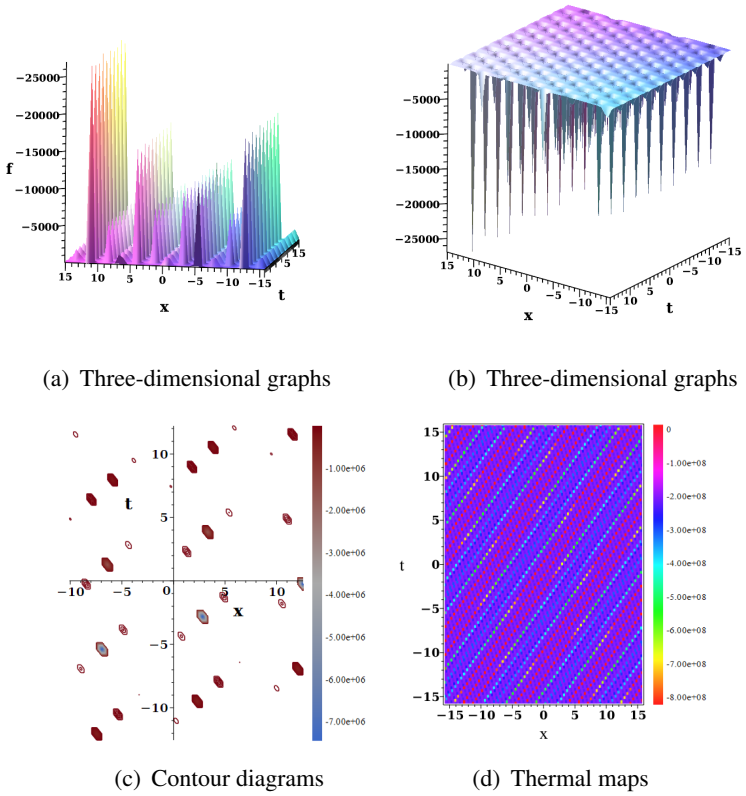

(a) Three-dimensional graphs (b) Three-dimensional graphs

(c) Contour diagrams (d) Thermal maps

Figure 7. Three-dimensional graphs, contour diagrams and thermal maps of Eq (3.19).

3.2.2. Model(4-3-1)-Case 2

In Model(4-3-1)-Case2, we try to use a bilinear neural network method to solve the equations. we derive the subsequent test function:

$$\begin{aligned} f = {} & b_4 + W_{1,u}\left[\operatorname{sech}\left(tW_{t,1} + xW_{x,1} + yW_{y,1} + zW_{z,1} + b_2\right)\right]^2 \\ & + W_{2,u}\sin\left(tW_{t,2} + xW_{x,2} + yW_{y,2} + zW_{z,1} + b_3\right) \\ & + W_{3,u}\,\wp\left(tW_{t,3} + xW_{x,3} + yW_{y,3} + zW_{z,1};\, g_2 = 1,\, g_3 = 1\right). \end{aligned} \tag{3.16}$$

Substituting Eq (3.16) into Eq (2.6), we can obtain

$$\begin{cases} b_4 = 0, \\ W_{1,u} = 0, \\ W_{2,u} = W_{2,u}, \\ W_{3,u} = 0, \\ W_{t,1} = W_{t,1}, \quad W_{t,2} = W_{t,2}, \quad W_{t,3} = W_{t,3}, \\ W_{x,1} = W_{x,1}, \quad W_{x,2} = W_{x,2}, \quad W_{x,3} = W_{x,3}, \\ W_{y,1} = W_{y,1}, \quad W_{y,3} = W_{y,3}, \\ W_{z,1} = W_{z,1}, \\ W_{y,2} = \dfrac{3(W_{x,2}^2 + W_{z,1}^2)}{W_{x,2}(4W_{x,2}^2 + 3)}. \end{cases} \tag{3.17}$$

Substituting Eq (3.17) into Eq (3.16), we obtain the solution of u, as follows:

$$u = w_{2,u}\sin\left(tw_{t,2} + xw_{x,2} + 3y\frac{w_{x,2}^2 + w_{z,1}^2}{w_{x,2}(4w_{x,2}^2 + 3)} + zw_{z,1} + b_3\right). \tag{3.18}$$

Substituting Eq (3.18) into Eq (2.4), we can get the expression of f as follows:

$$f = -2W_{x,2}^2\csc\left(tW_{t,2} + xW_{x,2} + 3y\frac{W_{x,2}^2 + W_{z,1}^2}{W_{x,2}(4W_{x,2}^2 + 3)} + zW_{z,1} + b_3\right)^2. \tag{3.19}$$

4. Two-hidden-layer model

4.1. Model(4-4-3-1)

4.1.1. Model(4-4-3-1)-Case 1

Departing from the single hidden layer architecture in Section 3, we develop a two-hidden-layer model (Figure 2c) maintaining four input neurons and one output neuron, while introducing a four-neuron first hidden layer, which are

$$\omega_1(v_1), \omega_2(v_2), \omega_3(v_3), \omega_4(v_4).$$

The second hidden layer consists of three neurons, which are

$$\omega_5(v_5), \omega_6(v_6), \omega_7(v_7).$$

Building upon the two-hidden-layer neural network architecture, we set the activation function in the hidden layer to

$$\begin{aligned} &\omega_1(v_1) = \cos(v_1), \quad \omega_2(v_2) = \sin(v_2), \quad \omega_3(v_3) = \tanh(v_3), \\ &\omega_4(v_4) = \operatorname{sech}(v_4), \quad \omega_5(v_5) = v_5^2, \quad \omega_6(v_6) = v_6^2, \quad \omega_7(v_7) = v_7^2. \end{aligned} \tag{4.1}$$

Employing an identical two-hidden-layer neural network architecture yields the subsequent test function:

$$\begin{aligned} f = b_8 + W_{5,\varnothing}\Big(&W_{1,5}\cos(tW_{t,1} + xW_{x,1} + yW_{y,1} + zW_{z,1} + b_1) \\ &+ W_{2,5}\sin(tW_{t,2} + xW_{x,2} + yW_{y,2} + zW_{z,2} + b_2) \\ &+ W_{3,5}\tanh(tW_{t,3} + xW_{x,3} + yW_{y,3} + zW_{z,3} + b_3) \\ &+ W_{4,5}\operatorname{sech}(tW_{t,4} + xW_{x,4} + yW_{y,4} + zW_{z,4} + b_4) + b_5\Big)^2 \\ +W_{6,\varnothing}\Big(&W_{1,6}\cos(tW_{t,1} + xW_{x,1} + yW_{y,1} + zW_{z,1} + b_1) \\ &+ W_{2,6}\sin(tW_{t,2} + xW_{x,2} + yW_{y,2} + zW_{z,2} + b_2) \\ &+ W_{3,6}\tanh(tW_{t,3} + xW_{x,3} + yW_{y,3} + zW_{z,3} + b_3) \\ &+ W_{4,6}\operatorname{sech}(tW_{t,4} + xW_{x,4} + yW_{y,4} + zW_{z,4} + b_4) + b_6\Big)^2 \\ +W_{7,\varnothing}\Big(&W_{1,6}\cos(tW_{t,1} + xW_{x,1} + yW_{y,1} + zW_{z,1} + b_1) \\ &+ W_{2,6}\sin(tW_{t,2} + xW_{x,2} + yW_{y,2} + zW_{z,2} + b_2) \\ &+ W_{3,6}\tanh(tW_{t,3} + xW_{x,3} + yW_{y,3} + zW_{z,3} + b_3) \\ &+ W_{4,6}\operatorname{sech}(tW_{t,4} + xW_{x,4} + yW_{y,4} + zW_{z,4} + b_4) + b_7\Big)^2. \end{aligned} \tag{4.2}$$

Substituting Eq (4.2) into Eq (1.1), we obtain the following solution:

$$\begin{cases} b_5 = b_5, & b_6 = b_6, & b_7 = b_7, & W_{1,5} = W_{1,5}, & W_{1,6} = W_{1,6}, & W_{2,5} = W_{2,5}, \\ W_{2,6} = 0, & W_{3,5} = W_{3,5}, & W_{3,6} = 0, & W_{4,5} = W_{4,5}, & W_{4,6} = W_{4,6}, & \\ W_{t,1} = 0, & W_{t,2} = 0, & W_{t,3} = -\dfrac{W_{z,3}^2}{W_{y,3}}, & W_{t,4} = -\dfrac{W_{z,4}^2}{W_{y,4}}, & & \\ W_{x,1} = 0, & W_{x,2} = 0, & W_{x,3} = 0, & W_{x,4} = 0, & & \\ W_{y,1} = 0, & W_{y,2} = 0, & W_{y,3} = W_{y,3}, & W_{y,4} = W_{y,4}, & & \\ W_{z,1} = 0, & W_{z,2} = 0, & W_{z,3} = W_{z,3}, & W_{z,4} = W_{z,4}, & & \\ W_{5,\varnothing} = 0, & W_{6,\varnothing} = W_{6,\varnothing}, & W_{7,\varnothing} = W_{7,\varnothing}. & & & \end{cases} \tag{4.3}$$

Substituting Eq (4.3) into Eq (4.2), we can obtain the solution to the initial equation, which is expressed as follows:

$$f = W_{6,\varnothing}\left(W_{1,6}\cos(b_1) + W_{4,6}\,\mathrm{sech}(A) + b_6\right)^2 + W_{7,\varnothing}\left(W_{1,6}\cos(b_1) + W_{4,6}\,\mathrm{sech}(A) + b_7\right)^2 + b_8,$$
$$A = \frac{-yW_{y,4}^2 + (-zW_{z,4} - b_4)W_{y,4} + tW_{z,4}^2}{W_{y,4}}. \tag{4.4}$$

This solution of Eq (4.4) is derived from a two-hidden-layer architecture (4-4-3-1) employing cosine and hyperbolic-secant activations, demonstrating the capacity of deeper networks to represent strongly nonlinear interactions. Physically, it models coherent structures such as soliton clusters in shallow-water waves or localized energy focusing in plasmas. The propagation direction of the localized wave structure is governed by the weights $W_{y,4}$ and $W_{z,4}$. The parameter $W_{4,6}$ scales the amplitude of the sech component, representing the strength of the nonlinearity. The bias term b_4 shifts the spatial position of the localized mode. Terms b_6 and b_7 introduce symmetric offsets, while b_8 sets a constant background level. Figure 8 depicts a highly localized, multi-peak waveform. The three-dimensional plot shows energy concentrated within a confined spatial region. Contour lines reveal a multi-lobed structure, and the corresponding heatmap identifies distinct high-intensity hotspots (red regions). The evolution diagram confirms that the localized wave packet propagates steadily along its trajectory, with nonlinear terms responsible for sustaining the focused energy distribution.

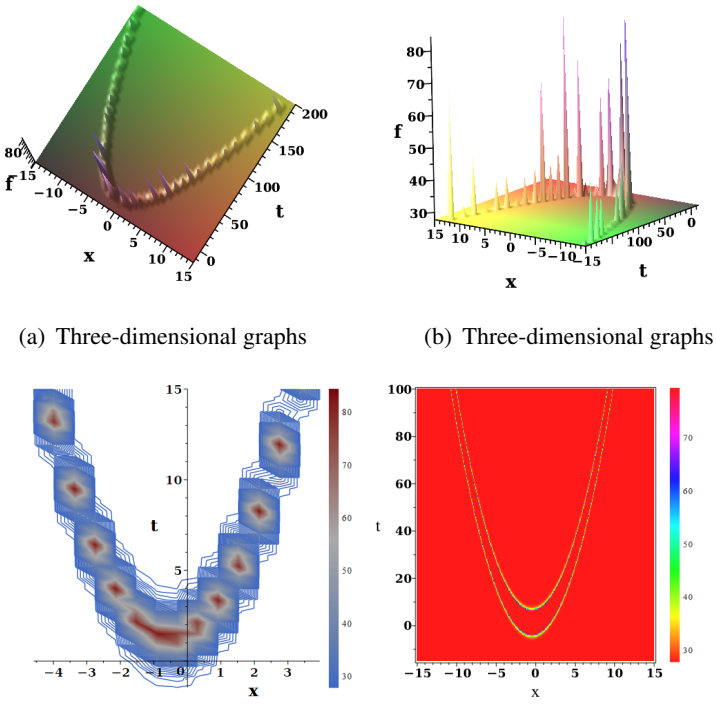

(a) Three-dimensional graphs (b) Three-dimensional graphs

(c) Contour diagrams (d) Thermal maps

Figure 8. Three-dimensional graphs, contour diagrams and thermal maps of Eq (4.4).

4.1.2. Model(4-4-3-1)-Case 2

In solving this subsection, we choose the same activation function as in Section 4.1.1 and obtain the same trial function. That is, the activation function in the neural network is still.

Hidden layer first layer:

$$\begin{aligned} &\omega_1(v_1) = \cos(v_1), \omega_2(v_2) = \sin(v_2), \\ &\omega_3(v_3) = \tanh(v_3), \omega_4(v_4) = \operatorname{sech}(v_4). \end{aligned} \tag{4.5}$$

Hidden layer second layer:

$$\omega_5(v_5) = (v_5)^2, \omega_6(v_6) = (v_6)^2, \omega_7(v_7) = (v_7)^2. \tag{4.6}$$

The resulting activation function remains:

$$\begin{aligned} f = {} & b_8 + W_{5,\varnothing}\Big(W_{1,5}\cos\Big(tW_{t,1} + xW_{x,1} + yW_{y,1} + zW_{z,1} + b_1\Big) \\ & + W_{2,5}\sin\Big(tW_{t,2} + xW_{x,2} + yW_{y,2} + zW_{z,2} + b_2\Big) + \\ & + W_{3,5}\tanh\Big(tW_{t,3} + xW_{x,3} + yW_{y,3} + zW_{z,3} + b_3\Big) + \\ & + W_{4,5}\operatorname{sech}\Big(tW_{t,4} + xW_{x,4} + yW_{y,4} + zW_{z,4} + b_4\Big) + b_5\Big)^2 + \\ & W_{6,\varnothing}\Big(W_{1,6}\cos\Big(tW_{t,1} + xW_{x,1} + yW_{y,1} + zW_{z,1} + b_1\Big) \\ & + W_{2,6}\sin\Big(tW_{t,2} + xW_{x,2} + yW_{y,2} + zW_{z,2} + b_2\Big) + \\ & + W_{3,6}\tanh\Big(tW_{t,3} + xW_{x,3} + yW_{y,3} + zW_{z,3} + b_3\Big) + \\ & + W_{4,6}\operatorname{sech}\Big(tW_{t,4} + xW_{x,4} + yW_{y,4} + zW_{z,4} + b_4\Big) + b_6\Big)^2 + \\ & W_{7,\varnothing}\Big(W_{1,6}\cos\Big(tW_{t,1} + xW_{x,1} + yW_{y,1} + zW_{z,1} + b_1\Big) \\ & + W_{2,6}\sin\Big(tW_{t,2} + xW_{x,2} + yW_{y,2} + zW_{z,2} + b_2\Big) + \\ & + W_{3,6}\tanh\Big(tW_{t,3} + xW_{x,3} + yW_{y,3} + zW_{z,3} + b_3\Big) + \\ & + W_{4,6}\operatorname{sech}\Big(tW_{t,4} + xW_{x,4} + yW_{y,4} + zW_{z,4} + b_4\Big) + b_7\Big)^2. \end{aligned} \tag{4.7}$$

Similarly, substituting Eq (4.7) into Eq (1.1) and performing symbolic calculations, we select the following solution during the calculation process:

$$\begin{cases} b_5 = b_5, & b_6 = b_6, & b_7 = b_7, \\ W_{1,5} = W_{1,5}, & W_{1,6} = W_{1,6}, & W_{2,5} = W_{2,5}, \\ W_{2,6} = W_{2,6}, & W_{3,6} = W_{3,6}, & W_{4,5} = W_{4,5}, \\ W_{4,6} = W_{4,6}, & W_{t,1} = 0, & W_{t,2} = 0, \\ W_{t,4} = W_{t,4}, & W_{x,1} = 0, & W_{x,2} = 0, \\ W_{x,3} = 0, & W_{x,4} = 0, & W_{y,1} = 0, \\ W_{y,2} = 0, & W_{y,4} = 0, & W_{z,1} = 0, \\ W_{z,2} = 0, & W_{z,4} = 0, & W_{5,\varnothing} = W_{5,\varnothing}, \\ W_{6,\varnothing} = W_{6,\varnothing}, & W_{7,\varnothing} = W_{7,\varnothing}, & \\ W_{t,3} = -\dfrac{W_{z,3}^2}{W_{y,3}}, & & \\ W_{3,5} = -\dfrac{W_{3,6}W_{4,6}(W_{6,\varnothing} + W_{7,\varnothing})}{W_{4,5}W_{5,\varnothing}}. & & \end{cases} \tag{4.8}$$

Substituting Eq (4.8) into Eq (4.7), we obtain the exact solution under the same activation function and probe function settings but with different parameters, whose analytical expression is given below:

$$\begin{aligned} f = {} & b_8 + \tfrac{1}{W_{5,\varnothing}W_{4,5}^2}\left(W_{3,6}W_{4,6}\left(W_{6,\varnothing} + W_{7,\varnothing}\right)\tanh\left(\tfrac{-yW_{y,3}^2+\left(-zW_{z,3}-b_3\right)W_{y,3}+tW_{z,3}^2}{W_{y,3}}\right)\right. \\ & +W_{4,5}W_{5,\varnothing}\left(W_{1,5}\cos\left(b_1\right) + W_{2,5}\sin\left(b_2\right) + +W_{4,5}\operatorname{sech}\left(tW_{t,4} + b_4\right) + b_5\right))^2 \\ & +W_{6,\varnothing}\left(W_{1,6}\cos\left(b_1\right) + W_{2,6}\sin\left(b_2\right) - W_{3,6}\tanh\left(\tfrac{-yW_{y,3}^2+\left(-zW_{z,3}-b_3\right)W_{y,3}+tW_{z,3}^2}{W_{y,3}}\right)\right. \\ & +W_{4,6}\operatorname{sech}\left(tW_{t,4} + b_4\right) + b_6\Big)^2 + +W_{7,\varnothing}\left(W_{1,6}\cos\left(b_1\right) + W_{2,6}\sin\left(b_2\right)\right. \\ & \left.-W_{3,6}\tanh\left(\tfrac{-yW_{y,3}^2+\left(-zW_{z,3}-b_3\right)W_{y,3}+tW_{z,3}^2}{W_{y,3}}\right)\right. \\ & \left.+W_{4,6}\operatorname{sech}\left(tW_{t,4} + b_4\right) + b_7\right)^2. \end{aligned} \tag{4.9}$$

Equation (4.9) represents a complex solution derived from the two-hidden-layer architecture (4-4-3-1), which incorporates tanh, sech, and cosine activation functions. The model demonstrates a capacity to describe strongly nonlinear localization phenomena. In physical contexts, it is applicable to the simulation of extreme rogue waves in ocean dynamics or to the modeling of soliton collisions in plasmas. Parameters such as $W_{z,3}$ govern the wavenumber, while $W_{3,6}$ scales the amplitude of the hyperbolic tangent (tanh) component, capturing the effect of nonlinear saturation.Bias terms, including b_3, influence the phase profile. Collectively, the multiple bias parameters tune the spatial symmetry of the solution and set the background field level. Figure 9 displays a non-periodic, multi-peak localized structure. The three-dimensional visualization reveals a waveform with several distinct amplitude peaks. The corresponding contour lines exhibit irregular wavefronts, and the heatmap identifies localized regions of high energy concentration. The evolution diagram confirms the structural stability of this coherent state, reflecting a strongly localized regime governed by dominant nonlinear interactions.

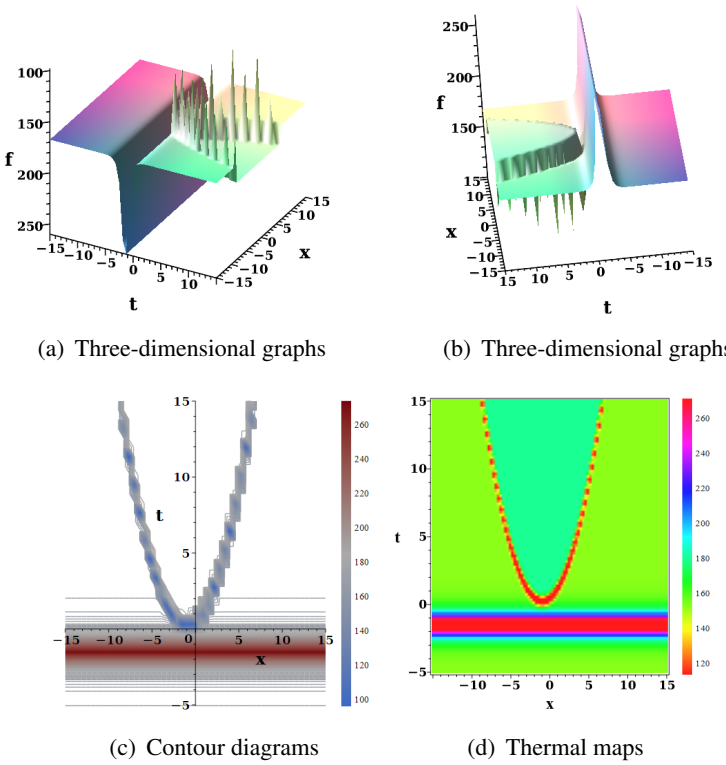

(a) Three-dimensional graphs (b) Three-dimensional graphs

(c) Contour diagrams (d) Thermal maps

Figure 9. Three-dimensional graphs, contour diagrams and thermal maps of Eq (4.9).

5. Conclusions

In this paper, we introduce the SANNA, a novel framework for solving PDEs. By integrating the efficient training capabilities of neural networks with the high precision of symbolic computation, this approach enables a more comprehensive analysis and deeper insights into PDE studies. Additionally, we combine the proposed model with the BNNM method to solve the Hirota bilinear equation, successfully deriving multiple new exact solutions. These solutions exhibit diverse behaviors, including periodic propagation driven by linear terms and localized pulse or energy concentration governed by nonlinear terms. This diversity highlights the versatility of the equation's solutions. By leveraging these solution behaviors, we can effectively describe or predict real-world physical scenarios under varying conditions.

Compared to traditional analytical and numerical methods for solving PDEs, the neural network combined with the symbolic computation model we propose is more convenient, requiring minimal theoretical analysis and computation, and does not demand advanced mathematical or physical theoretical knowledge. It is user-friendly for scholars new to this field and is simple and easy to understand.

In this article, we solve the Hirota bilinear equation. In fact, the Hirota bilinear equation can be considered a class of equations, and we solve one of them, successfully obtaining an exact solution. In fact, as long as the solution can be obtained through the Hirota bilinear transformation for various physical equations or methods in other fields, our proposed method can also solve them while ensuring

high accuracy. For example, in fluid mechanics, using the bilinear form of the Boussinesq equation describing water waves, the localized peak solutions we obtained can predict the instantaneous rise of sea waves, enabling relevant personnel to adjust strategies in a timely manner and assist researchers in optimizing marine engineering. Similarly, for optical field nonlinear Schrödinger equation light arc solutions, plasma physics field plasma waves, or plasma nonlinear waves, our proposed method can solve the equations to obtain the solution's form and characteristics, describe the solution's behavior, and apply it to real-world scenarios and predictions.

In summary, the presented approach exhibits robust computational performance in deriving exact solutions for nonlinear PDEs, offering valuable references and practical applications for optimizing solution speed and accuracy. It is anticipated that more scholars will adopt this method to explore broader research domains, thereby advancing the progress and development of the field of partial differential equation research.

Author contributions

Jianglong Shen: Conceptualization, Resources, Software, Funding acquisition, Writing-review & editing, Visualization, Project administration; Min Liu: Resource, Writing-original draft, Methodology; Jingbin Liang: Writing-original draft, Software, Visualization; Runfa Zhang: Conceptualization, Resources, Software, Methodology. All authors contributed equally to the preparation of this manuscript. All authors have read and approved the final version of the manuscript for publication.

Use of Generative-AI tools declaration

The authors declare they have not used Artificial Intelligence (AI) tools in the creation of this article.

Acknowledgments

This work was supported by the Open Research Fund of Computational Physics Key Laboratory of Sichuan Province, Yibin University (No. YBUJSWL-KX-2025-04), Yibin University Launch Project (No. 2024XJQH04), Yibin University Cultivation Project (No. 2024XJPY13).

Conflict of interest

The authors declare that they have no conflict of interest concerning the publication of this manuscript.

References

1. S. Tang, X. Feng, W. Wu, H. Xu, Physics-informed neural networks combined with polynomial interpolation to solve nonlinear partial differential equations, *Comput. Math. Appl.*, **132** (2023), 48–62. https://doi.org/10.1016/j.camwa.2022.12.008

2. J. Yong, X. Luo, S. Sun, C. Ye, Deep mixed residual method for solving PDE-constrained optimization problems, *Comput. Math. Appl.*, **176** (2024), 510–524. https://doi.org/10.1016/j.camwa.2024.11.009

3. G. Lei, Z. Lei, L. Shi, C. Zeng, D. Zhou, Solving PDEs on spheres with physics-informed convolutional neural networks, *Appl. Comput. Harmon. Anal.*, **74** (2025), 101714. https://doi.org/10.1016/j.acha.2024.101714

4. Z. Zhao, Y. Zhang, Periodic wave solutions and asymptotic analysis of the Hirota-Satsuma shallow water wave equation, *Math. Method. Appl. Sci.*, **38** (2015), 4262–4271. https://doi.org/10.1002/mma.3362

5. J. Chu, Y. Liu, W. Ma, Integrability and multiple-rogue and multi-soliton wave solutions of the (3+1)-dimensional Hirota-Satsuma-Ito equation, *Mod. Phys. Lett. B*, **39** (2025), 2550060. https://doi.org/10.1142/S0217984925500605

6. J. Shen, R. Zhang, J. Huang, J. Liang, Neural network-based symbolic computation algorithm for solving (2+1)-dimensional Yu-Toda-Sasa-Fukuyama equation, *Mathematics*, **13** (2025), 3006. https://doi.org/10.3390/math13183006

7. W. Huang, C. Zhou, X. Lü, J. Wang, Dispersive optical solitons for the Schrödinger-Hirota equation in optical fibers, *Mod. Phys. Lett. B*, **35** (2021), 2150060. https://doi.org/10.1142/S0217984921500603

8. Y. Wang, C. Temuer, Y. Yang, Integrability for the generalised variable-coefficient fifth-order Korteweg-de Vries equation with Bell polynomials, *Appl. Math. Lett.*, **29** (2014), 13–19. https://doi.org/10.1016/j.aml.2013.10.007

9. Y. Zhou, W. Ma, Applications of linear superposition principle to resonant solitons and complexitons, *Comput. Math. Appl.*, **73** (2017), 1697–1706. https://doi.org/10.1016/j.camwa.2017.02.015

10. L. Gao, Y. Zi, Y. Yin, W. Ma, X Lü, Bäcklund transformation, multiple wave solutions and lump solutions to a (3+1)-dimensional nonlinear evolution equation, *Nonlinear Dyn.*, **89** (2017), 2233–2240. https://doi.org/10.1007/s11071-017-3581-3

11. B. Ren, W. Ma, J. Yu, Characteristics and interactions of solitary and lump waves of a (2+1)-dimensional coupled nonlinear partial differential equation, *Nonlinear Dyn.*, **96** (2019), 717–727. https://doi.org/10.1007/s11071-019-04816-x

12. Z. Lan, Y. Gao, J. Yang, C. Su, C. Zhao, Z. Gao, Solitons and Bäcklund transformation for a generalized (3+1)-dimensional variable-coefficient B-type Kadomtsev-Petviashvili equation in fluid dynamics, *Appl. Math. Lett.*, **60** (2016), 96–100. https://doi.org/10.1016/j.aml.2016.03.021

13. Z. Lan, Y. Gao, C. Zhao, J. Yang, C. Su, Dark soliton interactions for a fifth-order nonlinear Schrödinger equation in a Heisenberg ferromagnetic spin chain, *Superlattices and Microstructures*, **100** (2016), 191–197. https://doi.org/10.1016/j.spmi.2016.09.022

14. L. Gao, X. Zhao, Y. Zi, J. Yu, X. Lü, Resonant behavior of multiple wave solutions to a Hirota bilinear equation, *Comput. Math. Appl.*, **72** (2016), 1225–1229. https://doi.org/10.1016/j.camwa.2016.06.008

15. W. Ma, Y. Zhang, Y. Tang, J. Tu, Hirota bilinear equations with linear subspaces of solutions, *Appl. Math. Comput.*, **218** (2012), 7174–7183. https://doi.org/10.1016/j.amc.2011.12.085

16. W. Li, A. Jiao, W. Liu, Z. Guo, High-order rational-type solutions of the analogous (3+1)-dimensional Hirota-bilinear-like equation, *Math. Biosci. Eng.*, **20** (2023), 19360–19371. https://doi.org/10.3934/mbe.2023856

17. Y. Ye, L. Wang, Z. Chang, J. He, An efficient algorithm of logarithmic transformation to Hirota bilinear form of KdV-type bilinear equation, *Appl. Math. Comput.*, **218** (2011), 2200–2209. https://doi.org/10.1016/j.amc.2011.07.036

18. H. Ismael, H. Nabi, T. Sulaiman, N. Shah, S. Eldin, H. Bulut, Hybrid and physical interaction phenomena solutions to the Hirota bilinear equation in shallow water waves theory, *Results Phys.*, **53** (2023), 106978. https://doi.org/10.1016/j.rinp.2023.106978

19. H. Zheng, W. Ma, X. Gu, Hirota bilinear equations with linear subspaces of hyperbolic and trigonometric function solutions, *Appl. Math. Comput.*, **220** (2013), 226–234. https://doi.org/10.1016/j.amc.2013.06.019

20. T. Yin, Z. Xing, J. Pang, Modified Hirota bilinear method to (3+1)-D variable coefficients generalized shallow water wave equation, *Nonlinear Dyn.*, **111** (2023), 9741–9752. https://doi.org/10.1007/s11071-023-08356-3

21. M. Dong, S. Tian, X. Yan, L. Zou, Solitary waves, homoclinic breather waves and rogue waves of the (3+1)-dimensional Hirota bilinear equation, *Comput. Math. Appl.*, **75** (2018), 957–964. https://doi.org/10.1016/j.camwa.2017.10.037

22. G. Zhu, H. Wang, Z. Mou, Y. Lin, Various solutions of the (2+1)-dimensional Hirota-Satsuma-Ito equation using the bilinear neural network method, *Chinese J. Phys.*, **83** (2023), 292–305. https://doi.org/10.1016/j.cjph.2023.03.016

23. M. Alquran, R. Alhami, Analysis of lumps, single-stripe, breather-wave, and two-wave solutions to the generalized perturbed-KdV equation by means of Hirota's bilinear method, *Nonlinear Dyn.*, **109** (2022), 1985–1992. https://doi.org/10.1007/s11071-022-07509-0

24. U. Mandal, S. Malik, S. Kumar, A. Das, A generalized (2+1)-dimensional Hirota bilinear equation: integrability, solitons and invariant solutions, *Nonlinear Dyn.*, **111** (2023), 4593–4611. https://doi.org/10.1007/s11071-022-08036-8

25. J. Guo, Y. Yao, H. Wang, T. Gu, Pre-training strategy for solving evolution equations based on physics-informed neural networks, *J. Comput. Phys.*, **489** (2023), 112258. https://doi.org/10.1016/j.jcp.2023.112258

26. F. Li, J. Wang, Y. Yang, Exact and Data-Driven lump wave solutions for the (3+1)-dimensional Hirota-Satsuma-Ito-like equation, *Symmetry*, **16** (2024), 1469. https://doi.org/10.3390/sym16111469

27. A. Bihlo, R. O. Popovych, Physics-informed neural networks for the shallow-water equations on the sphere, *J. Comput. Phys.*, **456** (2022), 111024. https://doi.org/10.1016/j.jcp.2022.111024

28. Y. Zhang, M. Wang, F. Zhang, Z. Chen, A solution method for differential equations based on Taylor PINN, *IEEE Access*, **11** (2023), 145020–145030. https://doi.org/10.1109/ACCESS.2023.3331330

29. M. R. Admon, N. Senu, A. Ahmadian, Z. A. Majid, S. Salahshour, A new modern scheme for solving fractal-fractional differential equations based on deep feedforward neural network with multiple hidden layer, *Math. Comput. Simulat.*, **218** (2024), 311–333. https://doi.org/10.1016/j.matcom.2023.11.002

30. M. L. Shahab, H. Susanto, Neural networks for bifurcation and linear stability analysis of steady states in partial differential equations, *Appl. Math. Comput.*, **483** (2024), 128985. https://doi.org/10.1016/j.amc.2024.128985

31. C. Yi, Y. Chen, X. Lan, Comparison on neural solvers for the Lyapunov matrix equation with stationary & nonstationary coefficients, *Appl. Math. Model.*, **37** (2013), 2495–2502. https://doi.org/10.1016/j.apm.2012.06.022

32. Z. Lan, N-soliton solutions, Bäcklund transformation and Lax pair for a generalized variable-coefficient cylindrical Kadomtsev-Petviashvili equation, *Appl. Math. Lett.*, **158** (2024), 109239. https://doi.org/10.1016/j.aml.2024.109239

33. Y. Shen, B. Tian, Bilinear auto-Bäcklund transformations and soliton solutions of a (3+1)-dimensional generalized nonlinear evolution equation for the shallow water waves, *Appl. Math. Lett.*, **122** (2021), 107301. https://doi.org/10.1016/j.aml.2021.107301

34. S. Kumar, B. Mohan, Bilinearization and new center-controlled N-rogue solutions to a (3+1)-dimensional generalized KdV-type equation in plasmas via direct symbolic approach, *Nonlinear Dyn.*, **112** (2024), 11373–11382. https://doi.org/10.1007/s11071-024-09626-4

35. K. Wang, H. Zhu, F. Shi, X. Liu, G. Wang, G. Li, Lump wave, breather wave and other abundant wave solutions to the (2+1)-dimensional Sawada-Kotera-Kadomtsev Petviashvili equation of fluid mechanics, *Pramana*, **99** (2025), 40. https://doi.org/10.1007/s12043-024-02884-2

36. K. Hosseini, F. Alizadeh, E. Hinçal, M. Ilie, M. S. Osman, Bilinear Bäcklund transformation, Lax pair, Painlevé integrability, and different wave structures of a 3D generalized KdV equation, *Nonlinear Dyn.*, **112** (2024), 18397–18411. https://doi.org/10.1007/s11071-024-09944-7

37. J. Manafian, Novel solitary wave solutions for the (3+1)-dimensional extended Jimbo-Miwa equations, *Comput. Math. Appl.*, **76** (2018), 1246–1260. https://doi.org/10.1016/j.camwa.2018.06.018

38. R. Zhang, S. Bilige, Bilinear neural network method to obtain the exact analytical solutions of nonlinear partial differential equations and its application to p-gBKP equation, *Nonlinear Dyn.*, **95** (2019), 3041–3048. https://doi.org/10.1007/s11071-018-04739-z

39. R. Zhang, M. Li, A. Cherraf, S. Vadyala, The interference wave and the bright and dark soliton for two integro-differential equation by using BNNM, *Nonlinear Dyn.*, **111** (2023), 8637–8646. https://doi.org/10.1007/s11071-023-08257-5

40. M. Isah, A. Yokus, D. Kaya, Exploring the influence of layer and neuron configurations on Boussinesq equation solutions via a bilinear neural network framework, *Nonlinear Dyn.*, **112** (2024), 13361–13377. https://doi.org/10.1007/s11071-024-09708-3

41. S. Zhang, G. Zhu, W. Huang, H. Wang, C. Yang, Y. Lin, Symbolic computation of analytical solutions for nonlinear partial differential equations based on bilinear neural network method, *Nonlinear Dyn.*, **113** (2025), 7121–7137. https://doi.org/10.1007/s11071-024-10715-7

42. M. Sharifi, S. Shojaei, Y. Ighris, I. El Glili, A. Mohammadi, A. Chamkha, et al., Statistical and machine learning approaches integrated with CFD for effective thermal conductivity prediction of NEPCMs in natural convection between horizontal concentric cylinders, *J. Energy Storage*, **141** (2026), 119340. https://doi.org/10.1016/j.est.2025.119340

43. M. Sharifi, A. Mohammadi, A. Chamkha, A. Aly, Hydrothermal and entropy generation analysis of mixed convection heat transfer in Couette-Poiseuille flow of a trihybrid nanofluid over a backward-facing step, *Int. J. Therm. Sci.*, **220** (2026), 110283. https://doi.org/10.1016/j.ijthermalsci.2025.110283

44. A. Hyder, H. Budak, A. Aly, S. Abdelsalam, Exploring fractional Bullen-type inequalities via second-derivative bounds and artificial neural networks, *Eng. Appl. Artif. Intel.*, **162** (2025), 110283. https://doi.org/10.1016/j.engappai.2025.112619

AIMS Press